Structural Health Monitoring
XX(X):1–15

Reprints and permission:
sagepub.co.uk/journalsPermissions.nav
DOI: 10.1177/ToBeAssigned
www.sagepub.com/
SAGE

Physics-Motivated Domain Adaptation for Smart Touch-Based Bolted Flange Looseness Detection Using Stress Wave Sensing, Frequency Response Functions, and Machine Learning

Himansu Shaw[1], Jian Chen[1] and Gangbing Song[1]

Abstract

Bolt looseness in flanged connections can compromise the structural integrity and safety of pipeline systems, particularly in subsea environments. Stress wave-based structural health monitoring combined with machine learning has shown promise for detecting bolt preload loss, but existing approaches typically assume training and testing data originate from the same structure. Deploying developed model across flanges of different geometries induces domain shift that substantially degrades model performance. This paper proposes a physics-motivated domain adaptation framework based on frequency response function (FRF) signal transformation for bolt looseness monitoring across flanges of different diameters. Rather than performing feature-level distribution alignment, the method performs signal-level adaptation by modeling each flange as a linear time-invariant system per bolt preload state and estimating its FRF via the H1 spectral estimator. A transformation based on the ratio of source and target FRFs maps stress wave signals into the target flange, after which Mel-frequency cepstral coefficient (MFCC) features are extracted and classified using a support vector machine (SVM). Critically, this framework substantially reduces the data collection burden on new structures: since large-diameter flanges predominate in field deployments but large-scale data collection there is often impractical, the method requires only a small target-structure calibration set to estimate its FRF, which is then used to transform signals from a data-rich source structure rather than collecting extensive labeled target data. The framework is evaluated across three cross-flange transfer scenarios: transfer between 6-inch and 9-inch diameter flanges in air, transfer between 6-inch and 9-inch diameter flanges underwater, and transfer between 4.25-inch and 5-inch diameter flanges underwater. Using only twelve calibration signals from each target structure, the method achieves 96.0%, 92.2%, and 91.9% 3-class classification accuracy across these three scenarios respectively (93.4% average), substantially outperforming no adaptation (32.3% average), a Domain-Adversarial Neural Network baseline (38.7% average), and a calibration-only classifier (71.3% average).

Keywords

Bolted flange looseness detection, physics-motivated domain adaptation, frequency response function, H_1 spectral estimator, signal-level transformation, Mel-frequency cepstral coefficients (MFCC), support vector machine (SVM), smart touch sensing, structural health monitoring, underwater sensing, transfer learning

Introduction

Bolted flange connections are among the most ubiquitous structural joining elements in industrial and subsea systems, serving as primary load-bearing and pressure-sealing interfaces in oil and gas pipelines, offshore wind turbine towers, pressure vessels, aerospace cabins, and chemical processing plants. Chen et al.[1] noted that bolted flange joints are prized for their good rigidity, convenient assembly and disassembly, and reliable connections across many structural fields. Despite their prevalence, these connections carry an inherent vulnerability: bolt looseness. Xie et al.[2] demonstrated that in subsea pipeline applications, cyclic loading from vortex-induced vibration combined with preload scatter from tensioning methods can significantly reduce bolt fatigue life and compromise joint integrity over extended service periods. Zhao et al.[3] established that stainless steel bolts clamping aluminium alloys under deep-sea ambient pressures of 110 MPa can experience up to a 40% reduction in preload, with direct implications for subsea flange sealing performance. Sebaey TA. et al.[4] further highlighted that in ultra-deepwater environments, thermally induced preload relaxation, differential material expansion, and hydrostatic pressure-driven contact stress redistribution collectively elevate the risk of micro-leakage under long-term service loading. Tai et al.[5] confirmed that the integrity of multi-bolted flanges is crucial for safety and operational efficiency across oil and gas, chemical processing, and water treatment industries. The consequences of bolt looseness are

[1]Department of Mechanical and Aerospace Engineering, University of Houston, Houston, TX, USA

Corresponding author:
Gangbing Song Department of Mechanical and Aerospace Engineering, University of Houston, Houston, TX 77204, USA.
Email: GSong@Central.UH.EDU

severe: direct leakage, structural degradation, and in critical infrastructure, catastrophic safety hazards. Early detection of bolt looseness is therefore not merely desirable but critical to preventing failures before they escalate into irreversible structural and safety consequences.

A diverse range of signal-based strategies have been investigated for bolt looseness detection. In the guided wave domain, Wang et al.[6] used a piezoelectric transducer array with two-stage machine learning to locate looseness and Sui et al.[7] combined shear-horizontal wave modelling with data-driven monitoring. Yang et al.[8] applied a wavelet packet transform with a large margin distribution machine for vibration-based detection under random excitation. In the percussion domain, Kong et al.[9] pioneered tap-and-listen monitoring, later refined by Yuan et al.[10] via empirical mode decomposition and by Wang et al.[11] through analytical impact-acoustic modelling. Direct measurement methods include strain gauges[12], fiber Bragg grating curvature sensors[13], and ultrasonic time-of-flight sensing[14]. In the vision-based domain, Wang et al.[15], Luo et al.[16], and Kong et al.[17] progressively improved image-based angle estimation using perspective correction and deep learning. For subsea applications, Jiang et al.[18] introduced touch-enabled robotic-finger sensing, the conceptual basis for the smart-touch gripper used here, while Sanli et al.[19] developed a carbon-nanotube piezoresistive washer sensor for real-time loosening torque detection.

Machine learning techniques have been extensively applied to bolt looseness monitoring, offering improved automation and sensitivity over threshold-based approaches. Wang et al.[20] established a foundational method coupling multivariate multiscale fuzzy entropy from PZT stress wave signals with a genetic algorithm-optimised least square support vector machine, showing that entropy-based complexity measures effectively capture the nonlinear dynamical changes induced by preload loss. Wang et al.[21] extended this line of work by decomposing PZT-received ultrasonic signals through singular spectrum analysis and mapping dynamic regularity via multiscale sample entropy. In the underwater domain, Wang et al.[22] introduced the Smart Crawfish concept, in which a subsea robot equipped with PZT transducers performs active sensing on pipeline flanges, extracting multiscale entropy features for a stacking-based ensemble classifier, while He et al.[23] explored underwater bolted connection looseness detection using percussion with a shallow machine learning algorithm.

Deep learning approaches have since been introduced to automate feature extraction and improve classification performance. For multi-bolt positioning, Chen et al.[24] constructed multivariate recurrence plots from stress waves to expose recursive dynamical attributes, classifying looseness positions via a multi-head attention CNN. Qin et al.[25] targeted micro-looseness in aircraft engine components using batch-normalised stacked autoencoders that converge rapidly while preserving feature integrity. Zhang et al.[26] proposed a one-dimensional deep CNN that takes free vibration signals directly as input, fusing feature extraction and classification into a single pipeline. Bridging both paradigms, Chen et al.[27] proposed the FM-ROCKET model, integrating deep learning feature extraction with shallow linear classification for submerged bolted flanges, to the authors' knowledge, the first documented approach to bolted flange looseness detection in a fully underwater environment.

Despite these advances, all methods above share a fundamental assumption: training and deployment data originate from the same or similar structural configurations, an assumption rarely satisfied in practice.

In real-world SHM deployments, variations in structural geometry, boundary conditions, material properties, sensor placement, and ambient medium can significantly alter the statistical distribution of measured vibration signals, leading to domain shift between training and deployment data. Bao and Li[28] identified this as a central open challenge in machine learning-based SHM, noting that models trained on one structure frequently fail to generalise to another. In bolted flange monitoring this problem is particularly acute: flanges of different bore sizes produce systematically different stress wave signatures, and variation in the ambient medium from air to subsea water modifies wave speed and damping in ways no single-structure classifier can anticipate. Gardner et al.[29] provided the first systematic treatment of domain adaptation in SHM, demonstrating that distribution alignment methods can realign source and target feature spaces to recover meaningful damage classification. Gardner et al.[30] demonstrated that no two structures generate feature data from the same distribution owing to manufacturing tolerances, sensor placement differences, and environmental exposure, circumstances directly applicable to subsea flange populations where no two installations are identical. These works establish that domain shift is a structural property of any SHM deployment where training and operational conditions diverge.

Existing domain adaptation approaches in SHM have converged on statistical feature-space alignment as the primary transfer mechanism. Giglioni et al.[31] applied joint domain adaptation and normal condition alignment to transfer damage labels across real bridges and finite element models. Giglioni et al.[32] extended this to geometrically distinct bridge configurations under varying temperature and damage conditions. Battu et al.[33] partially incorporated physical information by using finite element models as the labelled source domain, though the adaptation step itself remained a purely statistical distribution alignment. In the bolted structure domain, Chen et al.[34] introduced a multitask active sensing framework with substructure cross-domain transfer learning, applying adversarial domain adaptation to transfer a bolt looseness model from a substructure to an operationally distinct portal frame. In prior work by the present authors, Shaw et al.[35] proposed a few-shot centroid alignment domain adaptation (CADA) approach for air-to-water transfer learning in smart touch-based bolted flange looseness detection, demonstrating that centroid-based feature alignment can mitigate domain shift between different operating environments. Despite these advances, a fundamental gap persists: none of the existing approaches incorporate physical system dynamics directly into the transfer mechanism, relying instead on purely statistical feature-space alignment that cannot compensate for signal-level domain shift arising from differences in structural dynamics between source and target flanges. The present work addresses this gap through a physics-motivated signal-level transformation based on experimentally estimated

FRFs. Because the transformation is derived directly from the structural dynamics of the source and target flanges rather than learned from a large labeled dataset, it drastically reduces the data collection burden associated with deploying a monitoring model on a new flange, requiring only a small number of calibration signals from the target structure to estimate the FRF. To the best of the authors' knowledge, no prior study has applied physics-motivated transfer learning for cross-structure bolt looseness monitoring between flanges of different diameters, a scenario of direct practical relevance to subsea pipeline inspection systems, where flanges of varying bore sizes are routinely encountered across a single operator's asset base.

This paper proposes a physics-motivated domain adaptation framework based on H_1 estimator-based FRF signal transformation for cross-structure bolt looseness monitoring. Each flange is modeled as a linear time-invariant system, and its dynamic characteristics are captured through experimentally estimated FRFs obtained using chirp excitation signals applied to both the source and target flanges. A signal-level transformation based on the ratio of source and target FRFs maps vibration responses from the source flange domain to the target flange domain, enabling machine learning models trained on one structure to generalise to structurally different flanges. The proposed approach requires only a small number of labeled chirp excitation response measurements from the target flange for FRF estimation. The main contributions of this paper are as follows:

- A physics-motivated signal-level domain adaptation framework is proposed, in which the H_1 spectral estimator is used to characterise the dynamic behaviour of each flange system, and the resulting FRF ratio serves as a physically interpretable transfer function for cross-structure signal adaptation. To the best of the authors' knowledge, this is the first study to apply physics-motivated transfer learning for bolt looseness monitoring across flanges of different diameters, bridging the domain gap at the signal level rather than the feature level.
- The proposed framework is evaluated across three cross-structure transfer scenarios: (i) 6-inch to 9-inch flange diameter transfer in air, (ii) 6-inch to 9-inch flange diameter transfer underwater, and (iii) 4.25-inch to 5-inch flange diameter transfer underwater, demonstrating generalisability across different flange diameter combinations and operating media.
- A systematic comparison is provided against three baselines. A no-adaptation baseline uses no data from the target flange at all. A Domain-Adversarial Neural Network baseline uses target signals but not their torque labels. A third baseline is trained directly on the same twelve random calibration signals that the proposed method uses to estimate its FRF. Because this third baseline and the proposed method are given exactly the same twelve signals and differ only in how those signals are used, the comparison between them shows what the FRF transformation contributes on its own.

The remainder of this paper is organised as follows. The theoretical foundation for H_1 estimator-based FRF estimation and signal transformation is presented first, followed by the proposed physics-motivated domain adaptation methodology covering the training and test stages, MFCC feature extraction, and SVM classification. The experimental setup, smart-touch sensing system, and data acquisition procedure are then described, followed by the dataset arrangement across the three transfer scenarios. Classification results with comparisons against the no-adaptation and DANN baselines are subsequently reported and discussed. The paper closes with concluding remarks and directions for future work.

Theoretical Foundation

Frequency Response Function Estimation

Accurate estimation of the frequency response function (FRF) is fundamental to characterizing the dynamic behavior of structural systems. In this study, each bolted flange assembly is modeled as a linear time-invariant (LTI) system excited by a controlled input signal $x(t)$ and producing a corresponding response signal $y(t)$. In the frequency domain, the input-output relationship of the system can be expressed as:

$$Y(\omega) = H(\omega)\,X(\omega) + N(\omega), \tag{1}$$

where $X(\omega)$ and $Y(\omega)$ are the Fourier transforms of the input and output signals, respectively, $H(\omega)$ is the true FRF of the system, and $N(\omega)$ represents measurement noise. Since noise is inevitably present in experimental measurements, the true FRF $H(\omega)$ cannot be computed directly from Equation (1). Instead, spectral estimators based on power spectral densities are used to obtain a reliable estimate of the FRF in the presence of noise. The auto-power spectral density of the input signal $G_{xx}(\omega)$, the auto-power spectral density of the output signal $G_{yy}(\omega)$, the cross-power spectral density between the output and input signals $G_{yx}(\omega)$, and the cross-power spectral density between the input and output signals $G_{xy}(\omega)$ are defined as:

$$G_{xx}(\omega) = \mathbb{E}\left[X(\omega)\,X^*(\omega)\right], \tag{2}$$

$$G_{yy}(\omega) = \mathbb{E}\left[Y(\omega)\,Y^*(\omega)\right], \tag{3}$$

$$G_{yx}(\omega) = \mathbb{E}\left[Y(\omega)\,X^*(\omega)\right], \tag{4}$$

$$G_{xy}(\omega) = \mathbb{E}\left[X(\omega)\,Y^*(\omega)\right], \tag{5}$$

where $(\cdot)^*$ denotes the complex conjugate and $\mathbb{E}[\cdot]$ denotes the expected value operator, estimated in practice by averaging over multiple signal realizations.

H_1 *Estimator*

The H_1 estimator is derived under the assumption that measurement noise is present primarily in the output signal $y(t)$, while the input signal $x(t)$ is relatively noise-free. Under this assumption, the output signal can be written as:

$$Y(\omega) = H(\omega)\,X(\omega) + N(\omega), \tag{6}$$

where $N(\omega)$ represents output noise uncorrelated with the input. Multiplying both sides of Equation (6) by $X^*(\omega)$ and taking the expected value yields:

$$G_{yx}(\omega) = H(\omega)\,G_{xx}(\omega) + \mathbb{E}\left[N(\omega)\,X^*(\omega)\right]. \tag{7}$$

Since the noise $N(\omega)$ is assumed to be uncorrelated with the input $X(\omega)$, the term $\mathbb{E}[N(\omega)\,X^*(\omega)] = 0$. The H_1

estimator is therefore obtained as:

$$\hat{H}_1(\omega) = \frac{G_{yx}(\omega)}{G_{xx}(\omega)}. \tag{8}$$

The H_1 estimator minimizes the effect of output noise and is known to provide a lower-bound estimate of the true FRF magnitude when noise is present in both input and output signals.

H_2 Estimator

The H_2 estimator is derived under the complementary assumption that measurement noise is present primarily in the input signal $x(t)$, while the output signal $y(t)$ is relatively noise-free. In this case, the input signal is modeled as:

$$X(\omega) = X_0(\omega) + M(\omega), \tag{9}$$

where $X_0(\omega)$ is the true noise-free input and $M(\omega)$ represents input noise uncorrelated with the output. The system equation in terms of the true noise-free input is therefore:

$$Y(\omega) = H(\omega)\, X_0(\omega) = H(\omega)\big[X(\omega) - M(\omega)\big]. \tag{10}$$

Multiplying both sides of Equation (10) by $Y^*(\omega)$ and taking the expected value yields:

$$\mathbb{E}\left[Y(\omega)\, Y^*(\omega)\right] = H(\omega)\,\mathbb{E}\left[X(\omega)\, Y^*(\omega)\right] - H(\omega)\,\mathbb{E}\left[M(\omega)\, Y^*(\omega)\right]. \tag{11}$$

Recognizing the spectral density definitions, Equation (11) can be written as:

$$G_{yy}(\omega) = H(\omega)\, G_{xy}(\omega) - H(\omega)\,\mathbb{E}\left[M(\omega)\, Y^*(\omega)\right]. \tag{12}$$

Since the input noise $M(\omega)$ is assumed to be uncorrelated with the output $Y(\omega)$, the term $\mathbb{E}[M(\omega)\, Y^*(\omega)] = 0$, and Equation (12) simplifies to:

$$G_{yy}(\omega) = H(\omega)\, G_{xy}(\omega). \tag{13}$$

Solving for $H(\omega)$, the H_2 estimator is therefore obtained as:

$$H_2(\omega) = \frac{G_{yy}(\omega)}{G_{xy}(\omega)}. \tag{14}$$

The H_2 estimator provides an upper-bound estimate of the true FRF magnitude and minimizes the effect of input noise.

Selection of the H_1 Estimator Over the H_2 Estimator for FRF-Based Domain Adaptation

In practical experimental measurements, noise is generally present in both the input and output signals. However, in the active sensing configuration adopted in this study, the excitation signal is generated by a controlled NI PXI-based signal generation system and amplified through a TREK high-voltage amplifier before being applied to the PZT (Lead Zirconate Titanate) actuator. This controlled excitation process ensures that the input signal maintains a high signal-to-noise ratio compared to the measured response signal, which is more susceptible to structural noise, sensor coupling variability, and the acoustic properties of the surrounding water medium. Since the dominant source of measurement uncertainty resides in the output signal rather than the input, the H_1 estimator is adopted in this study. The H_1 estimator, defined as the ratio of the cross-power spectral density of the input and output to the auto-power spectral density of the input, is specifically formulated to minimize the effect of noise present in the output signal, making it the more appropriate choice over the H_2 estimator for the present experimental configuration.

FRF-Based Signal Transformation

Each bolted flange assembly is modeled as a linear time-invariant (LTI) system, where the dynamic behavior of the structure is fully characterized by its frequency response function. As illustrated in Figure 1, the same chirp excitation signal $x(t)$ is applied to both the source and target flanges, producing structurally distinct response signals $y_1(t)$ and $y_2(t)$ that reflect the unique dynamic characteristics of each flange geometry.

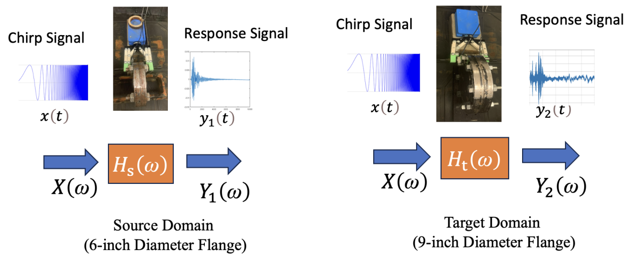

Figure 1. LTI modeling of the source (6-inch) and target (9-inch) flange systems under chirp excitation $x(t)$, with responses $y_1(t)$ and $y_2(t)$ characterized by FRFs $H_s(\omega)$ and $H_t(\omega)$ estimated via the H_1 spectral estimator.

LTI System Modeling of Flange Structures

In this work, each bolted flange system is approximated as an LTI system within the excitation frequency range of interest. Under this assumption, the frequency-domain relationship between the excitation signal and the structural response is time-invariant and can be expressed through the FRF. When a chirp excitation signal $x(t)$ is applied to a flange structure, the corresponding response signal $y(t)$ can be related to the input in the frequency domain as:

$$Y(\omega) = H(\omega)\, X(\omega), \tag{15}$$

where $X(\omega) = \mathcal{F}\{x(t)\}$ and $Y(\omega) = \mathcal{F}\{y(t)\}$ are the Fourier transforms of the input and output signals, respectively, and $H(\omega)$ is the FRF of the system. The LTI assumption is well justified in this study because the chirp excitation signal operates at low amplitudes relative to the structural stiffness of the flange assembly, ensuring that the response remains in the linear regime across all bolt preload conditions tested.

The FRF encodes the complete dynamic signature of the flange structure, including its resonance frequencies, damping characteristics, and modal amplitudes, all of which are directly influenced by the flange geometry and boundary conditions. Critically, bolt preload also influences the dynamic stiffness and damping of the assembly, so the

FRF is itself a function of the bolt torque state. Consequently, flanges with different diameters *and* different preload conditions exhibit distinct FRFs, which is the fundamental source of domain shift between signals collected from different flange configurations.

Class-Conditioned Source and Target FRF Estimation

Two flange systems are considered in this study: a source flange (smaller diameter) and a target flange (larger diameter). Because bolt preload measurably alters the dynamic stiffness and damping of the flange assembly, a single global FRF per flange is insufficient to characterize the system across all bolt states. Instead, the FRF estimation is performed in a *class-conditioned* manner: separate FRFs are estimated for each bolt torque class $c \in \{0, 20, 40\}$ ft·lbs, yielding class-specific estimates $H_s^{(c)}(\omega)$ and $H_t^{(c)}(\omega)$ for the source and target flanges, respectively.

Applying the LTI system model of Equation (15) to each system and each torque class, the ideal class-conditioned FRFs are defined as:

$$H_s^{(c)}(\omega) = \frac{Y_1^{(c)}(\omega)}{X(\omega)}, \tag{16}$$

$$H_t^{(c)}(\omega) = \frac{Y_2^{(c)}(\omega)}{X(\omega)}, \tag{17}$$

where $Y_1^{(c)}(\omega)$ and $Y_2^{(c)}(\omega)$ are the Fourier transforms of the source and target response signals measured under torque class c, and $X(\omega)$ is the common chirp excitation sweeping from 1 kHz to 60 kHz over a duration of 500 ms.

In practice, $H_s^{(c)}(\omega)$ and $H_t^{(c)}(\omega)$ are estimated from experimental measurements using the H_1 spectral estimator.

$$H_s^{(c)}(\omega) = \frac{G_{y_1x}^{(c)}(\omega)}{G_{xx}^{(c)}(\omega) + \varepsilon}, \tag{18}$$

$$H_t^{(c)}(\omega) = \frac{G_{y_2x}^{(c)}(\omega)}{G_{xx}^{(c)}(\omega) + \varepsilon}, \tag{19}$$

where $G_{y_1x}^{(c)}(\omega)$ and $G_{y_2x}^{(c)}(\omega)$ are the cross-power spectral densities between the respective response signals and the excitation signal under torque class c, $G_{xx}^{(c)}(\omega)$ is the auto-power spectral density of the excitation signal, and $\varepsilon = 10^{-18}$ is a small regularization constant added to ensure numerical stability at anti-resonance frequencies where $G_{xx}^{(c)}(\omega) \approx 0$.

The H_1 estimator is implemented using a Hann window of length $N_{\mathrm{w}} = 8192$ samples with 50% overlap ($N_{\mathrm{ov}} = 4096$ samples), with mean detrending applied to each segment. Given a sampling frequency of $f_s = 1$ MHz, this yields a frequency resolution of $\Delta f = f_s/N_{\mathrm{w}} \approx 122$ Hz across the excitation band. For each torque class and each flange system, four distinct signal repetitions are collected. Each repetition yields its own independent $H_1(\omega)$ estimate via Equation (8), so that four class-conditioned FRF pairs $\{H_s^{(c)}(\omega), H_t^{(c)}(\omega)\}$, $r = 1, \ldots, 4$, are obtained per torque class. Each of the four resulting transfer operators $R_r^{(c)}(\omega)$ is applied to the *entire* source dataset independently, producing four separately transformed copies of the source data, which are pooled to form the SVM training set. This increases the effective training set size fourfold relative to the raw source dataset and exposes the classifier to four distinct realizations of the transfer operator, rather than committing to a single estimate that may be sensitive to which particular calibration repetition was drawn.

The estimated class-conditioned FRF magnitude plots for the source and target flanges across all three transfer scenarios are shown in Figures 4, 3, and 2, where the representative case of $c = 0$ ft·lbs is displayed for visualization purposes. The distinct resonance patterns observed between the source and target FRFs in each scenario confirm the presence of significant domain shift arising from differences in flange geometry, and motivate the need for the class-conditioned signal-level transformation described in the following subsection.

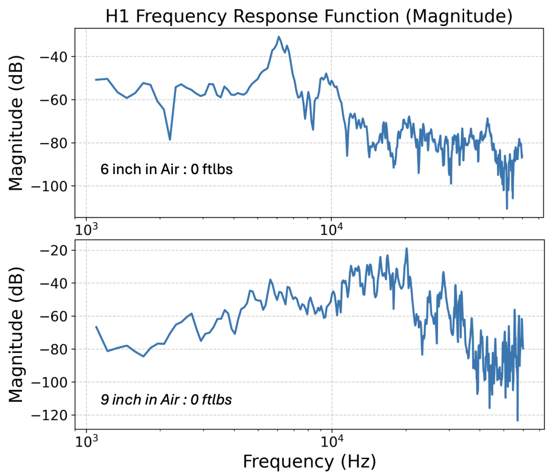

(c) Air: 6-inch → 9-inch

Figure 2. Estimated class-conditioned FRF magnitude plot $|H_t^{(c)}(\omega)|$ for the air 6-inch to 9-inch diameter flange transfer scenario.

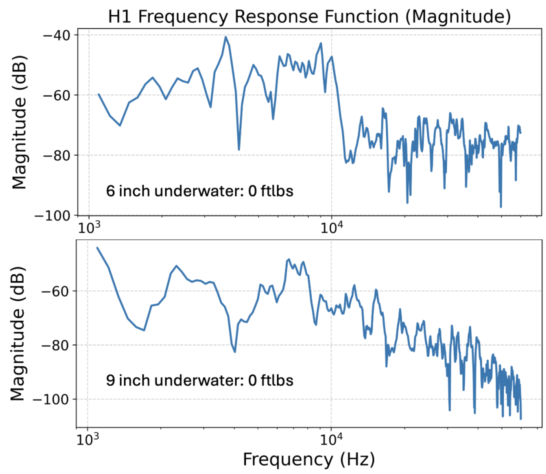

(b) Water: 6-inch → 9-inch

Figure 3. Estimated class-conditioned FRF magnitude plot $|H_s^{(c)}(\omega)|$ for the underwater 6-inch to 9-inch diameter flange transfer scenario.

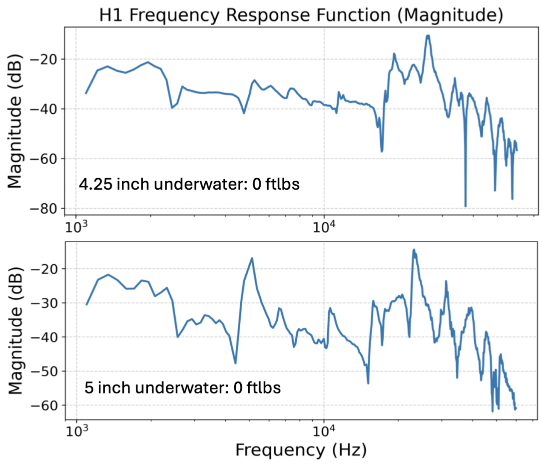

(a) Water: 4.25-inch → 5-inch

Figure 4. Estimated class-conditioned FRF magnitude plot $|H_s^{(c)}(\omega)|$ for the underwater 4.25-inch to 5-inch diameter flange transfer scenario.

Class-Conditioned Frequency-Domain Signal Transformation

The core idea of the proposed domain adaptation framework is to exploit the experimentally estimated class-conditioned FRFs to perform a signal-level transformation that maps vibration responses from the source flange domain to the target flange domain. Given a response signal $y_1^{(c)}(t)$ collected from the source flange under bolt torque class c, its frequency-domain representation is obtained as:

$$Y_1^{(c)}(\omega) = \mathcal{F}\{y_1^{(c)}(t)\}. \tag{20}$$

Using the LTI system model of Equation (15), the source response can be expressed as $Y_1^{(c)}(\omega) = H_s^{(c)}(\omega)\,X(\omega)$. If the same excitation $X(\omega)$ had been applied to the target flange under the same torque class c, the ideal target response would be $Y_2^{(c)}(\omega) = H_t^{(c)}(\omega)\,X(\omega)$. The ratio of these two expressions eliminates the excitation $X(\omega)$:

$$\frac{Y_2^{(c)}(\omega)}{Y_1^{(c)}(\omega)} = \frac{H_t^{(c)}(\omega)\,X(\omega)}{H_s^{(c)}(\omega)\,X(\omega)} = \frac{H_t^{(c)}(\omega)}{H_s^{(c)}(\omega)}. \tag{21}$$

This leads directly to the proposed class-conditioned FRF ratio transfer operator:

$$R^{(c)}(\omega) = \frac{H_t^{(c)}(\omega)}{H_s^{(c)}(\omega)}, \tag{22}$$

which encodes the dynamic difference between the target and source flanges at torque class c. Rearranging Equation (21), the ideal target response can be expressed as:

$$\hat{Y}_2^{(c)}(\omega) = Y_1^{(c)}(\omega) \cdot R^{(c)}(\omega), \tag{23}$$

where $\hat{Y}_2^{(c)}(\omega)$ is a reconstructed signal in the frequency–domain - not a real measurement of the target flange, but a synthetic approximation constructed by spectrally reshaping the real source signal $Y_1^{(c)}(\omega)$ through the FRF ratio filter $R^{(c)}(\omega)$. The hat notation $(\hat{\cdot})$ is used throughout to emphasize that this is a model-based reconstruction rather than a direct measurement. The time-domain transformed signal is recovered via the inverse Fourier transform:

$$\hat{y}_2^{(c)}(t) = \mathcal{F}^{-1}\left\{\hat{Y}_2^{(c)}(\omega)\right\}. \tag{24}$$

The class-conditioned formulation is essential for physical consistency: applying $R^{(c)}(\omega)$ to source signals of class c accounts for the preload-dependent dynamic stiffness and damping of both flanges at that torque state, eliminating the modeling error that would arise from assuming FRF invariance across preload levels.

The transformed signal $\hat{y}_2^{(c)}(t)$ replaces actual target measurements during training, allowing the SVM to be trained on data approximating the target flange dynamics without requiring labeled target measurements beyond the small FRF calibration set.

Figure 5 presents a representative comparison of the real source signal, real target signal, and FRF-reconstructed target signal for all three transfer scenarios at the 0 ft-lbs (loose) bolt preload condition. As observed, the reconstructed 5-inch, 9-inch (underwater), and 9-inch (air) responses closely replicate the temporal structure and amplitude envelope of their respective real target signals, confirming that the class-conditioned FRF ratio transformation effectively bridges the domain gap between source and target flange systems.

Proposed Methodology

The proposed physics-motivated domain adaptation framework enables cross-structure bolt looseness monitoring by transforming source flange vibration signals into the target flange domain using experimentally estimated FRFs. As illustrated in Figure 6, the framework operates in two stages: a training stage, in which FRF-transformed source signals are used to train an SVM classifier, and a test stage, in which raw target signals are classified by the trained SVM model.

Training Stage: FRF-Based Signal Transformation

The signal transformation block constitutes the core of the proposed framework. Each source signal $y_1^{(c)}(t)$ undergoes the following three-step procedure to produce its reconstructed target-domain counterpart $\hat{y}_2^{(c)}(t)$.

Step 1 FFT. The source signal is converted to the frequency domain:

$$Y_1^{(c)}(\omega) = \mathcal{F}\left\{y_1^{(c)}(t)\right\}. \tag{25}$$

Step 2 FRF Ratio Multiplication. The frequency-domain signal is multiplied by the class-conditioned FRF ratio:

$$R^{(c)}(\omega) = \frac{H_t^{(c)}(\omega)}{H_s^{(c)}(\omega)}, \tag{26}$$

where $H_s^{(c)}(\omega)$ and $H_t^{(c)}(\omega)$ are the H_1 estimator-based FRFs of the source and target flanges at torque class c, as defined in Equations (18) and (19). The reconstructed target-domain signal in the frequency domain is then:

$$\hat{Y}_2^{(c)}(\omega) = Y_1^{(c)}(\omega) \cdot \frac{H_t^{(c)}(\omega)}{H_s^{(c)}(\omega)}. \tag{27}$$

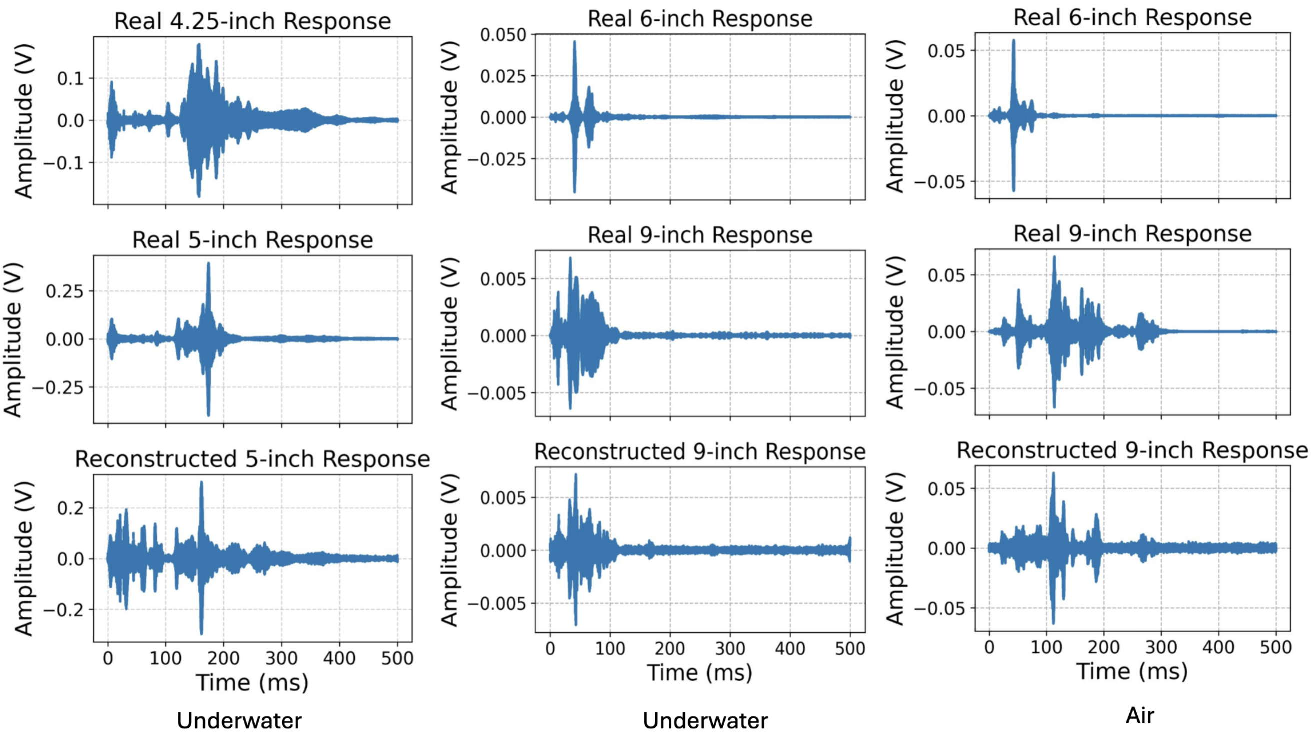

Figure 5. Comparison of real source, real target, and FRF-reconstructed target signals across three cross-structure transfer scenarios: (left) Underwater: 4.25-inch $\rightarrow$ 5-inch diameter flange, (center) Underwater: 6-inch $\rightarrow$ 9-inch diameter flange, (right) Air: 6-inch $\rightarrow$ 9-inch diameter flange. The reconstructed signals closely approximate the real target responses across all scenarios.

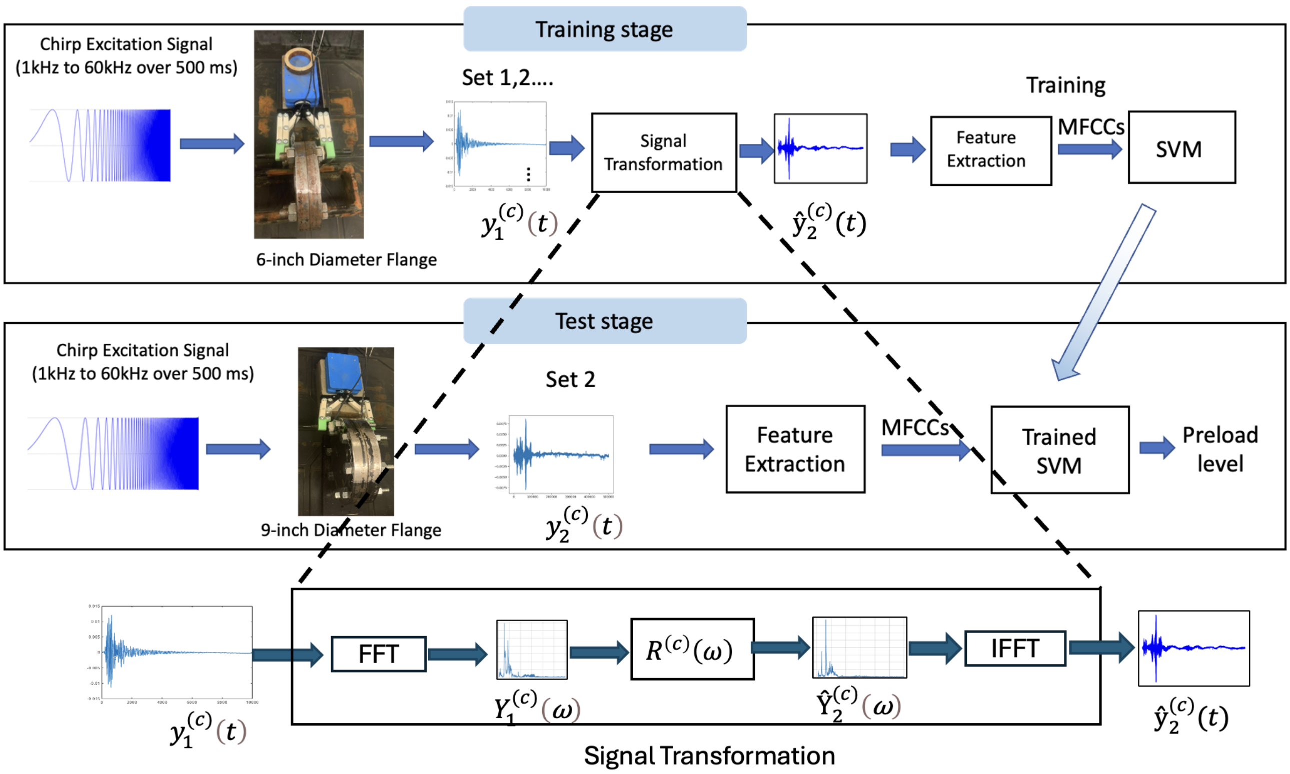

Figure 6. Overview of the proposed physics-motivated domain adaptation framework showing the training stage, test stage, and signal transformation detail.

Step 3 IFFT. The time-domain reconstructed signal is recovered via the inverse Fourier transform:

$$\hat{y}_2^{(c)}(t) = \mathcal{F}^{-1}\left\{\hat{Y}_2^{(c)}(\omega)\right\}. \tag{28}$$

The signal $\hat{y}_2^{(c)}(t)$ is subsequently used for MFCC feature extraction and SVM classifier training.

Test Stage

In the test stage, the chirp excitation signal is applied to the target flange and the resulting stress-wave response $y_2^{(c)}(t)$ is recorded. The raw target signal is passed directly through the MFCC feature extraction pipeline, and the extracted feature vector is classified using the SVM model trained on transformed source signals.

Feature Extraction: Mel-Frequency Cepstral Coefficients (MFCCs)

MFCC features are extracted from both the transformed training signals $\hat{y}_2^{(c)}(t)$ and the raw test signals $y_2^{(c)}(t)$ to provide a compact and noise-robust spectral representation of the stress-wave responses. The extraction procedure is illustrated in Figure 7 and follows five sequential steps.

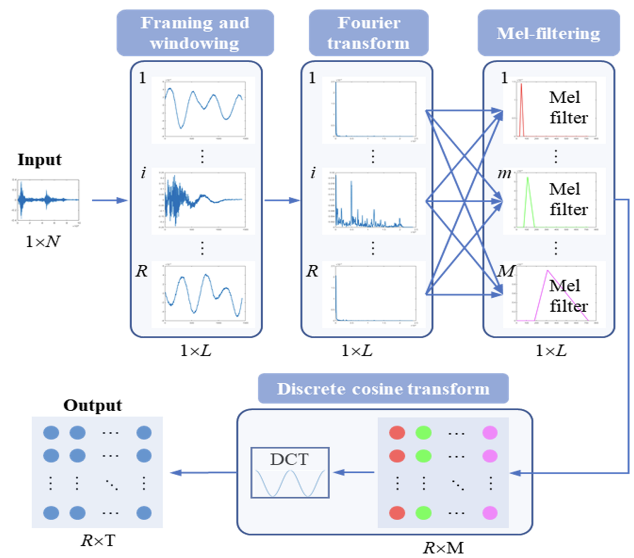

Figure 7. Flowchart of the MFCC feature extraction procedure.

Each signal is first segmented into short overlapping frames, and a Hamming window is applied to each frame to suppress spectral leakage at frame boundaries. An FFT is then computed on each windowed frame to obtain its magnitude spectrum, which is subsequently passed through a bank of triangular bandpass filters spaced on the Mel frequency scale. The Mel scale applies a nonlinear frequency mapping that emphasizes lower-frequency components where dominant structural resonances and mechanical responses are typically concentrated. The filter bank outputs are converted to the logarithmic scale to compress the dynamic range and improve robustness to amplitude variations caused by differences in transducer coupling conditions between repeated measurements. Finally, a Discrete Cosine Transform (DCT) is applied to the log-Mel filter bank energies to decorrelate the features and produce a compact set of orthogonal coefficients. The first $C = 20$ MFCC coefficients are retained per frame, producing a two-dimensional feature tensor of shape $[C \times T]$, where T is the number of frames, which is flattened into a one-dimensional feature vector and passed to the SVM classifier.

Classification: Support Vector Machine

The extracted MFCC feature vectors are classified using a Support Vector Machine (SVM) with a Radial Basis Function (RBF) kernel. SVM is selected for its strong generalization performance in high-dimensional feature spaces with relatively small training datasets, a critical property in the cross-structure transfer setting where training data is limited to transformed source signals. A one-versus-one (OvO) multiclass strategy is adopted to handle the three-class bolt preload classification problem (0, 20, and 40 ft-lbs). The RBF kernel is defined as:

$$K(\mathbf{x}_i, \mathbf{x}_j) = \exp\left(-\gamma \, \|\mathbf{x}_i - \mathbf{x}_j\|^2\right), \tag{29}$$

where $\gamma > 0$ is the kernel bandwidth parameter. The regularization parameter $C = 1$.

Domain-Adversarial Neural Network Baseline

The Domain-Adversarial Neural Network (DANN)[36] is implemented as a representative of feature-level statistical alignment, the paradigm against which the proposed signal-level adaptation is positioned. DANN comprises a feature extractor $G_f(\cdot\,; \theta_f)$, a label predictor $G_y(\cdot\,; \theta_y)$ that classifies bolt preload condition, and a domain discriminator $G_d(\cdot\,; \theta_d)$ that determines whether a feature vector originated from the source or target flange. Given labeled source samples and unlabeled target samples, the three components are trained jointly on

$$E(\theta_f, \theta_y, \theta_d) = \mathcal{L}_y(\theta_f, \theta_y) - \lambda\, \mathcal{L}_d(\theta_f, \theta_d), \tag{30}$$

where $\mathcal{L}_y$ is the cross-entropy label loss over source samples, $\mathcal{L}_d$ is the cross-entropy domain-classification loss over source and target samples, and $\lambda > 0$ weights the adversarial term. The label predictor and feature extractor minimize E while the discriminator maximizes it, driving the extractor to produce features from which the domain of origin cannot be recovered. This saddle-point optimization is realized in a single backward pass by a gradient reversal layer (GRL) placed between G_f and G_d, which is the identity in the forward direction and negates the gradient in the backward direction:

$$\mathcal{R}(\mathbf{z}) = \mathbf{z}, \qquad \frac{\partial \mathcal{R}(\mathbf{z})}{\partial \mathbf{z}} = -\lambda \mathbf{I}. \tag{31}$$

Following Ganin et al.[36], λ is annealed from 0 to 1 as $\lambda_p = 2/(1 + \exp(-\gamma p)) - 1$ with $\gamma = 10$ and p the fraction of training completed, preventing the adversarial term from destabilizing the network before the label predictor has converged.

DANN therefore assumes that a representation aligning the marginal feature distributions $p_s(\mathbf{z})$ and $p_t(\mathbf{z})$ also preserves the class-conditional structure $p(y \mid \mathbf{z})$. Section examines the consequences when this assumption does not hold.

The baseline is implemented following Ganin et al.[36] and receives the same MFCC input representation as all other methods in this study, computed from raw signals with no FRF transformation applied. Source-domain training data comprises all labeled sets of the source flange. Target-domain data comprises one unlabeled set from the target flange, selected in each fold to be disjoint from the test set and identified explicitly in Tables 8-10. No target labels are used at any stage of DANN training.

Experimental Setup and Procedure

Smart Touch-Based Sensing System

A robotic gripper integrated with a spring–plunger-based smart-touch mechanism is employed to ensure repeatable and controlled contact between the Lead Zirconate Titanate (PZT) transducers and the flange surface, as illustrated in Figure 8. The mechanism compensates for surface irregularities and maintains consistent coupling conditions across repeated measurements, without requiring permanent sensor bonding. PZT is a widely used piezoceramic material exhibiting a strong piezoelectric effect, commonly applied for both actuation and sensing of stress waves in structural health monitoring systems. In the active sensing configuration adopted in this study, a linear chirp excitation sweeping from 1 kHz to 60 kHz over 500 ms is applied to one PZT element acting as an actuator, while a second PZT element serves as a sensor to capture the transmitted stress wave response in the time domain. Since wave propagation through the flange assembly is governed by bolt preload and joint stiffness, the recorded signal is processed into a Mel-frequency cepstral coefficient (MFCC) matrix, which captures variations in spectral energy distribution associated with different torque states.

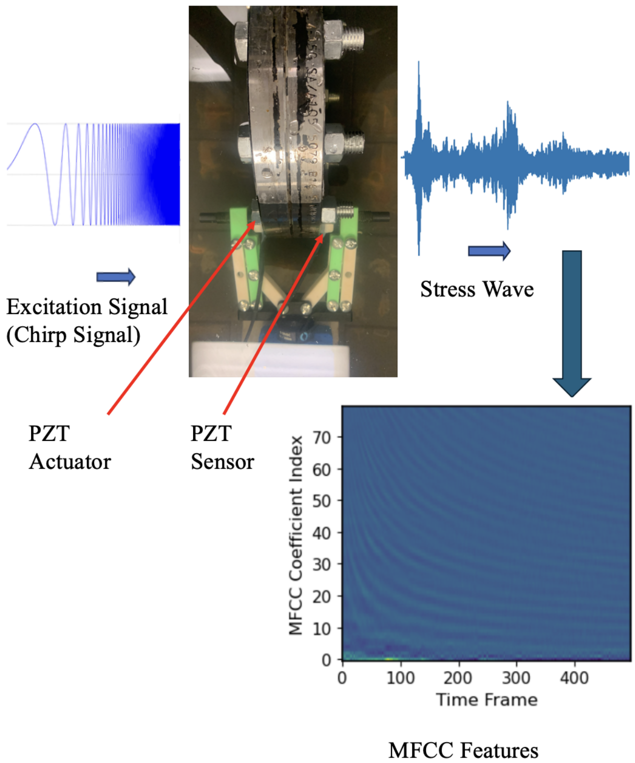

Figure 8. Illustration of the active sensing process, showing chirp excitation, stress wave propagation through the bolted flange joint, recorded vibration response, and the corresponding MFCC feature representation.

Four bolted flange specimens of different diameters are used in this study 9-inch, 6-inch, 5-inch, and 4.25-inch as shown in Figure 9. These define three cross-structure transfer scenarios: (i) 6-inch to 9-inch in air, (ii) 6-inch to 9-inch underwater, and (iii) 4.25-inch to 5-inch underwater. Scenarios (i) and (ii) involve the same flange pair but are treated as independent setups since the water medium significantly alters stress-wave propagation characteristics, producing distinct signal distributions. Scenario (iii) further assesses generalizability across a different flange pair with a smaller geometric difference.

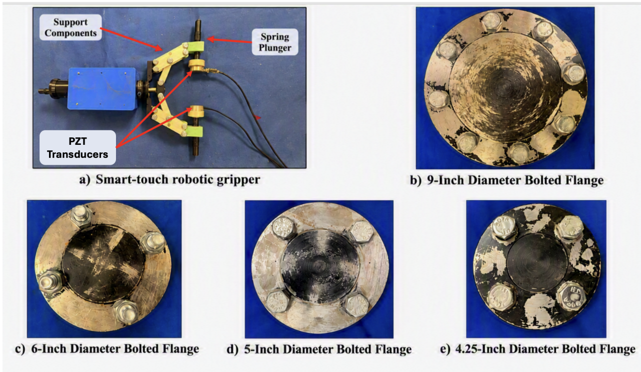

Figure 9. Pictures of the smart-touch robotic gripper and bolted flange specimens used in this study. (a) Smart-touch robotic gripper equipped with a PZT transducers, support components, and spring plungers. (b) 9-inch diameter bolted flange. (c) 6-inch diameter bolted flange. (d) 5-inch diameter bolted flange. (e) 4.25-inch diameter bolted flange.

The experimental platform is shown in Figure 10. The system comprises a host PC running a LabVIEW-based control interface, a National Instruments PXI-based data acquisition and signal generation system (NI PXI-1042), a TREK high-voltage amplifier, and a microcontroller-controlled robotic gripper with PZT transducers. The NI PXI unit simultaneously generates the chirp excitation and acquires the sensor response at a sampling rate of 1 MHz, with the excitation amplified through the high-voltage amplifier to drive the PZT actuator.

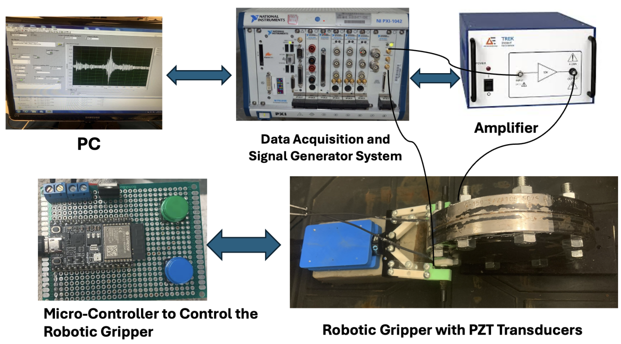

Figure 10. Experimental platform for smart touch-based stress-wave sensing of bolted flange joints, including the host PC with LabVIEW control, NI PXI-based data acquisition and signal generation system, high-voltage amplifier, microcontroller-based gripper controller, and robotic gripper equipped with PZT transducers.

Dataset Arrangement

To evaluate the proposed FRF-based domain adaptation framework, vibration datasets were collected from four bolted flange structures of different diameters under controlled experimental conditions. Three cross-structure transfer scenarios are considered, each defined by a source flange, a target flange, and an operating medium. For each flange configuration, vibration signals were recorded under three bolt preload conditions: 0 ft-lbs (loose), 20 ft-lbs (moderately tightened), and 40 ft-lbs (fully tightened). For every preload level, 40 samples were collected per dataset, yielding 120 samples per dataset. The three scenarios are described below.

Scenario I: 6-inch to 9-inch Flange Transfer in Air

In Scenario I, signals collected from the 6-inch flange in air constitute the source domain, while signals from the 9-inch flange in air constitute the target domain. Five datasets (Sets 1–5) were collected from the 6-inch flange, and four datasets (Sets 1–4) were collected from the 9-inch flange, as summarized in Tables 1 and 2.

Table 1. Dataset distribution for the 6-inch flange in air (source domain, Scenario I).

Set	0 ft-lbs	20 ft-lbs	40 ft-lbs	Sample count
Set 1	40	40	40	120
Set 2	40	40	40	120
Set 3	40	40	40	120
Set 4	40	40	40	120
Set 5	40	40	40	120

Table 2. Dataset distribution for the 9-inch flange in air (target domain, Scenario I).

Set	0 ft-lbs	20 ft-lbs	40 ft-lbs	Sample count
Set 1	40	40	40	120
Set 2	40	40	40	120
Set 3	40	40	40	120
Set 4	40	40	40	120

Scenario II: 6-inch to 9-inch Flange Transfer Underwater

In Scenario II, the same 6-inch to 9-inch flange transfer is evaluated under underwater conditions. Although the flange pair is identical to Scenario I, the surrounding water medium significantly alters the stress-wave propagation characteristics, resulting in distinct signal distributions compared to the air environment. This scenario is therefore treated as an independent experimental setup. Four datasets (Sets 1–4) were collected from the 6-inch flange underwater, and three datasets (Sets 1–3) were collected from the 9-inch flange underwater, as summarized in Tables 3 and 4.

Table 3. Dataset distribution for the 6-inch flange underwater (source domain, Scenario II).

Set	0 ft-lbs	20 ft-lbs	40 ft-lbs	Sample count
Set 1	40	40	40	120
Set 2	40	40	40	120
Set 3	40	40	40	120
Set 4	40	40	40	120

Table 4. Dataset distribution for the 9-inch flange underwater (target domain, Scenario II).

Set	0 ft-lbs	20 ft-lbs	40 ft-lbs	Sample count
Set 1	40	40	40	120
Set 2	40	40	40	120
Set 3	40	40	40	120

Scenario III: 4.25-inch to 5-inch Flange Transfer Underwater

In Scenario III, domain transfer is performed between a 4.25-inch flange (source) and a 5-inch flange (target) under underwater conditions. Three datasets (Sets 1–3) were collected from each flange configuration, as summarized in Tables 5 and 6.

Table 5. Dataset distribution for the 4.25-inch flange underwater (source domain, Scenario III).

Set	0 ft-lbs	20 ft-lbs	40 ft-lbs	Sample count
Set 1	40	40	40	120
Set 2	40	40	40	120
Set 3	40	40	40	120

Table 6. Dataset distribution for the 5-inch flange underwater (target domain, Scenario III).

Set	0 ft-lbs	20 ft-lbs	40 ft-lbs	Sample count
Set 1	40	40	40	120
Set 2	40	40	40	120
Set 3	40	40	40	120

Results and Discussion

The proposed FRF-based domain adaptation framework is evaluated across the three cross-structure transfer scenarios described in the preceding section. In all scenarios the SVM classifier is trained exclusively on FRF-transformed source signals and tested on raw vibration signals collected directly from the target flange. Three baselines are reported, chosen to isolate the contribution of each component of the framework.

Baseline 1: No adaptation. An SVM trained on MFCC features from raw source signals is applied directly to raw target signals. This baseline uses no target-domain data and quantifies the severity of the domain shift.

Baseline 2: DANN. The Domain-Adversarial Neural Network[36] learns domain-invariant representations by adversarially aligning the source and target distributions in a shared feature space. It is trained on labeled raw source signals together with *unlabeled* raw target signals, optimizing a label classifier and a domain discriminator simultaneously; through gradient reversal the feature extractor is driven to confuse the discriminator. The unlabeled adaptation set used in each fold is disjoint from the test set and is identified in the results tables. This baseline represents statistical feature-level alignment and receives

120 unlabeled target samples per fold, with no target labels at any stage.

Baseline 3: Calibration-only. An SVM is trained directly on the calibration set, 12 signals in total, four per torque class, and evaluated on the target test sets. These are the same 12 signals the proposed method uses to estimate $\hat{H}_t^{(c)}(\omega)$. The two methods therefore start from identical target-domain data and differ only in how it is used: here the 12 signals are the entire training set, while the proposed method uses them to build a transfer operator that is applied to the full source dataset. This comparison isolates what the FRF transformation adds beyond simply training on the calibration set directly.

Table 7 summarizes the target-domain data consumed by each method. The three preload conditions,0 ft-lbs (loose), 20 ft-lbs (moderately tightened) and 40 ft-lbs (fully tightened),are referred to as Class 0, Class 1 and Class 2 throughout. All methods use the identical MFCC pipeline and, where applicable, identical SVM hyperparameters.

Table 7. Data consumed by each method.

Method	Labeled source	Labeled target	Unlabeled target
No adaptation	All	0	0
DANN	All	0	120
Target-only	0	12	-
Proposed (FRF)	All	12	-

Scenario I: 6-inch to 9-inch Flange Transfer in Air

The classifier is trained on FRF-transformed signals from the 6-inch flange (Sets 1–5) and evaluated on four independent datasets from the 9-inch flange in air. Results are summarized in Table 8.

The proposed method achieves 95.8%, 97.5%, 93.3% and 97.5% across the four test sets, averaging 96.0%. The no-adaptation baseline averages 31.2%, below random chance for a three-class problem (33.3%), confirming severe domain shift between the 6-inch and 9-inch flanges. DANN averages 33.5%, indistinguishable from chance despite 120 unlabeled target samples per fold, and in two of the four folds performs *below* the no-adaptation baseline, indicating that adversarial alignment is not merely insufficient here but can be counterproductive. The target-only baseline averages 67.3%, confirming that the 12 labeled signals carry genuine discriminative information; the proposed method nevertheless exceeds it by 28.7 percentage points, and does so in every fold. Since both consume the same 12 signals, this margin is attributable entirely to the FRF transformation.

Confusion matrices for the proposed method are shown in Figure 11. Class 0 (loose) is classified perfectly across all four sets. Residual errors fall into two groups: confusions between Class 1 and Class 2, physically consistent since adjacent preload levels produce more similar responses; and a small number of Class 2 samples assigned to Class 0 (two in Set 1, three in Set 2, one in Set 4), which are conservative errors that would trigger unnecessary inspection rather than pass a loose joint.

Scenario II: 6-inch to 9-inch Flange Transfer Underwater

Scenario II evaluates the same flange pair underwater. The classifier is trained on FRF-transformed signals from the 6-inch flange (Sets 1–4) and evaluated on three datasets from the 9-inch flange, as summarized in Table 9.

The proposed method achieves 90.0%, 90.8% and 95.8%, averaging 92.2%. The no-adaptation and DANN baselines average 34.9% and 36.7%, both at or near chance, confirming that the domain shift is equally severe underwater and that adversarial alignment again provides negligible benefit. The target-only baseline reaches 64.7%, and the proposed method exceeds it by 27.5 percentage points.

The target-only baseline varies widely across folds here (55.8–74.1%), whereas the proposed method spans only 90.0–95.8% on the same folds.

Confusion matrices are shown in Figure 12. Compared with Scenario I, more Class 1/Class 2 confusions appear, particularly in Sets 1 and 2, consistent with the more challenging acoustic environment. Class 0 remains perfectly classified across all three sets.

Scenario III: 4.25-inch to 5-inch Flange Transfer Underwater

Scenario III evaluates a different flange pair underwater. The classifier is trained on FRF-transformed signals from the 4.25-inch flange (Sets 1–3) and evaluated on three datasets from the 5-inch flange, as summarized in Table 10.

The proposed method achieves 95.8%, 90.0% and 90.0%, averaging 91.9%, against 30.7% without adaptation. Both adaptive baselines perform markedly better here than in Scenarios I and II, DANN reaches 46.0% and the target-only baseline 82.0%, consistent with the smaller geometric difference between the 4.25-inch and 5-inch flanges producing a milder domain shift that is partially amenable to statistical alignment and that leaves the calibration signals closer in distribution to the test data.

The margin over the baseline is correspondingly smallest here at 9.9 percentage points, against 28.7 and 27.5 points in Scenarios I and II. This is the expected behavior: the benefit of signal-level transformation scales with the structural difference between source and target. Where the gap is small, training directly on the calibration set is already competitive; where it is large, the regime of practical interest, since the motivating deployment transfers from a small laboratory flange to a much larger field flange, the transformation becomes essential. The proposed method remains best-performing in all three scenarios. Confusion matrices are shown in Figure 13. Errors in Sets 2 and 3 are again concentrated between Class 1 and Class 2. Class 0 is identified correctly in 115 of 120 cases, with four samples assigned to Class 1 and one to Class 2.

Baseline Failure Modes and Comparative Analysis

No-adaptation confusion matrices for Set 1 of each scenario are shown in Figure 14. Predictions are heavily biased toward one or two classes regardless of the true preload state. In Scenarios II and III the classifier never

Table 8. Classification results for Scenario I: 6-inch to 9-inch flange transfer in air. The DANN adaptation set is the unlabeled target-domain set used for adversarial alignment in each fold, disjoint from the test set.

Training	Testing	No Adapt.	DANN		Target-Only	FRF
			Adaptation set (unlabeled)	Acc.	(Calibration samples)	
Sets 1–5	Set 1	25.8%	Set 3	33.0%	66.7%	95.8%
Sets 1–5	Set 2	40.8%	Set 3	39.0%	67.5%	97.5%
Sets 1–5	Set 3	35.8%	Set 4	33.0%	69.1%	93.3%
Sets 1–5	Set 4	22.5%	Set 3	29.0%	65.8%	97.5%
Average		31.2%	-	33.5%	67.3%	**96.0%**

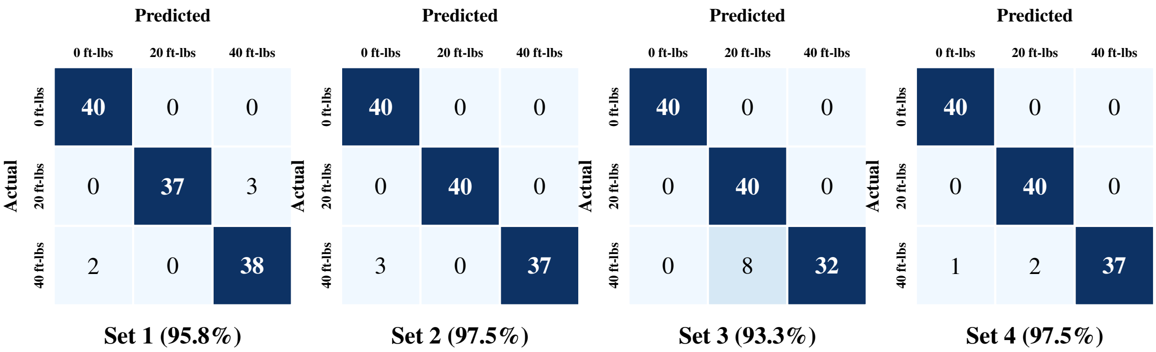

Figure 11. Confusion matrices for Scenario I (Air: 6-inch to 9-inch flange transfer) using the proposed FRF-based method. Class 0 = 0 ft-lbs, Class 1 = 20 ft-lbs, Class 2 = 40 ft-lbs.

Table 9. Classification results for Scenario II: 6-inch to 9-inch flange transfer underwater.

Training	Testing	No Adapt.	DANN		Target-Only	FRF
			Adaptation set (unlabeled)	Acc.	(Calibration samples)	
Sets 1–4	Set 1	38.3%	Set 2	33.0%	55.8%	90.0%
Sets 1–4	Set 2	33.3%	Set 1	44.0%	74.1%	90.8%
Sets 1–4	Set 3	33.3%	Set 1	33.0%	64.1%	95.8%
Average		34.9%	-	36.7%	64.7%	**92.2%**

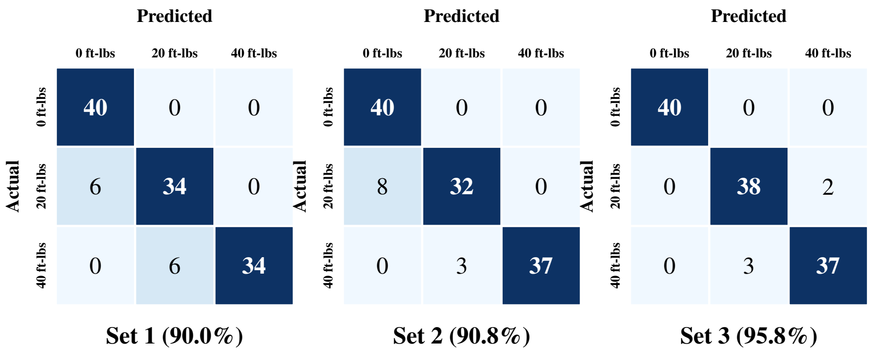

Figure 12. Confusion matrices for Scenario II (Water: 6-inch to 9-inch flange transfer) using the proposed FRF-based method. Class 0 = 0 ft-lbs, Class 1 = 20 ft-lbs, Class 2 = 40 ft-lbs.

predicts Class 2 at all: all 120 test samples, including the 40 fully tightened ones, are assigned to Class 0 or Class 1. This collapse of an entire decision region shows that the failure is not degraded accuracy but source-trained boundaries being geometrically inapplicable to the target feature space.

Against these failure modes, Table 11 consolidates the results. The proposed framework exceeds 90% average accuracy in all three scenarios and outperforms every baseline in every scenario.

Table 10. Classification results for Scenario III: 4.25-inch to 5-inch flange transfer underwater.

Training	Testing	No Adapt.	DANN		Target-Only	FRF
			Adaptation set (unlabeled)	Acc.	(Calibration samples)	
Sets 1–3	Set 1	35.0%	Set 2	37.0%	80.0%	95.8%
Sets 1–3	Set 2	33.0%	Set 1	47.0%	81.0%	90.0%
Sets 1–3	Set 3	24.0%	Set 1	54.0%	85.0%	90.0%
Average		30.7%	-	46.0%	82.0%	**91.9%**

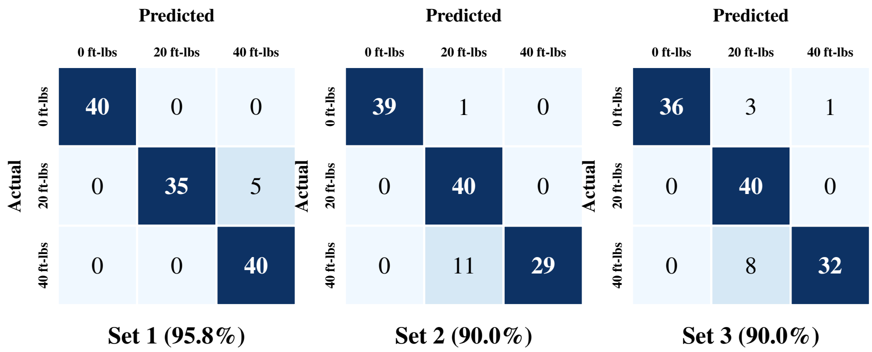

Figure 13. Confusion matrices for Scenario III (Water: 4.25-inch to 5-inch flange transfer) using the proposed FRF-based method. Class 0 = 0 ft-lbs, Class 1 = 20 ft-lbs, Class 2 = 40 ft-lbs.

Table 11. Summary of average classification accuracies across all three transfer scenarios, with target-domain supervision in parentheses.

Scenario	Medium	No Adapt.	DANN	Target-Only	FRF
Scenario I: 6-inch → 9-inch	Air	31.2%	33.5%	67.3%	**96.0%**
Scenario II: 6-inch → 9-inch	Water	34.9%	36.7%	64.7%	**92.2%**
Scenario III: 4.25-inch → 5-inch	Water	30.7%	46.0%	82.0%	**91.9%**
Mean across scenarios		32.3%	38.7%	71.3%	**93.4%**

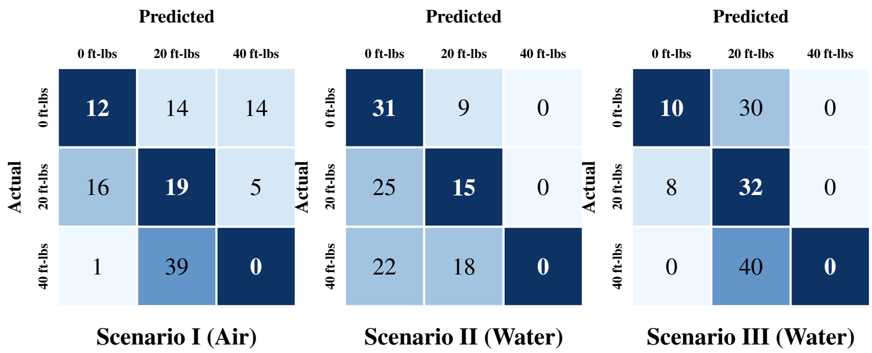

Figure 14. No-adaptation baseline confusion matrices for Set 1 of each transfer scenario. Note the complete absence of Class 2 predictions in Scenarios II and III.

The comparison against the target-only baseline is the most informative, because it holds the labeled target budget fixed. Averaged across scenarios the baseline reaches 71.3% and the proposed method 93.4%, a margin of 22.1 percentage points from identical calibration data. The 12 labeled signals are therefore best used not as training examples but as an estimate of the target system's dynamic response, which can then reshape a large volume of existing source data. In effect the class-conditioned FRF ratio converts a 12-sample target dataset into a target-domain training set.

Conclusion

This paper developed a physics-motivated domain adaptation framework for bolt looseness monitoring across bolted flange structures of different diameters, targeting practical SHM deployments in subsea and offshore environments. The core challenge is domain shift: a classifier trained on one flange degrades sharply when applied to a structurally different flange, and the no-adaptation baseline confirmed this shift is severe across all scenarios, with accuracy near random chance (30–35%).

The framework models each flange as a linear time-invariant system at each bolt preload state and estimates its FRF via the H_1 spectral estimator applied to chirp excitation. A class-conditioned FRF ratio transformation maps source flange vibration signals into the target flange domain, from which MFCC features are extracted and classified using an SVM. The transfer operator carries no trainable parameters and is determined entirely by two measured FRFs, giving the framework a physically interpretable and inspectable transfer mechanism. The sensing system uses a robotic smart-touch gripper with PZT transducers, enabling repeatable, non-invasive stress-wave interrogation without permanent sensor bonding.

Across the three transfer scenarios, 6-inch to 9-inch in air, 6-inch to 9-inch underwater, and 4.25-inch to 5-inch underwater, the framework achieved average accuracies of 96.0%, 92.2% and 91.9%, outperforming all three baselines in every one of the ten evaluation folds. The decisive comparison is against the baseline trained directly on the same 12 random calibration signals used for FRF estimation: the proposed method exceeds it by 9.9 to 28.7 percentage points depending on scenario (mean 22.1), a margin attributable to the FRF transformation rather than to the calibration data itself. This margin grows with the geometric difference between source and target, which is the regime of greatest practical interest. The fully loose condition was identified with 98.8% recall (395 of 400) across all ten test sets.

Future work includes replacing experimental FRF estimation with a finite element flange model to eliminate physical calibration, studying sensitivity to noise and averaging, finer preload increments for incipient looseness detection, extension to additional flange geometries and bolt configurations (including large-to-small transfer), and integration with uncertainty quantification for safety-critical deployment.

Acknowledgment

Study concept, oversight, and funding were provided by the U.S. Department of the Interior, Bureau of Safety and Environmental Enforcement (BSEE), Office of Offshore Regulatory Program Branch, Sterling, VA under Contract Number 140E0123C0007. The content, statements, findings, opinions, conclusions, and recommendations are those of the author(s) and do not necessarily reflect the views of the Bureau of Safety and Environmental Enforcement.

ORCID iDs

Himansu Shaw https://orcid.org/0009-0008-2845-6241
Jian Chen https://orcid.org/0000-0003-3678-4030
Gangbing Song https://orcid.org/0000-0001-5135-5555

References

[1] Chen X, Han W and Zhang Z. Loosening state monitoring and identification of multi-bolted flange joints based on nonlinear wave energy transmission. *Mech Syst Signal Process*. 2025;224:112114.

[2] Xie H, Zeng W, Zhu D, Sun W and Song H. Effect of preload scatter on fatigue life of subsea pipeline connector bolts located at suspended span section. *Proc Inst Mech Eng Part M J Eng Marit Environ*. 2025;239(2):313–321.

[3] Zhao Y, Zhang Y, Wang J, Yue Q and Chen H. Investigation of the variation in bolt preload force under deep-sea high ambient pressure. *J Mar Sci Eng*. 2026;14(2):131.

[4] Sebaey TA. Comprehensive study and analysis of tapping and nut bolt joints used in subsea applications. *J Manuf Mater Process*. 2026;10(4):120.

[5] Tai JL, Sultan MTH, Lukaszewicz A, Siemiatkowski Z, Skorulski G and Shahar FS. Preventing catastrophic failures: a review of applying acoustic emission testing in multi-bolted flanges. *Metals*. 2025;15(4):438.

[6] Wang W, Li A, Fan Y and Li L. Detecting bolt looseness of flanged joint based on multiple-mode conversion. *Struct Health Monit*. 2026;25(1):350–375.

[7] Sui X, Zhang R, Luo Y and Fang Y. Multiple bolt looseness detection using SH-typed guided waves: integrating physical mechanism with monitoring data. *Ultrasonics*. 2025;150:107601.

[8] Yang W, Zhang Z and Chen X. Vibration-based looseness identification of bolted structures via quasi-analytic wavelet packet and optimized large margin distribution machine. *Struct Health Monit*. 2024;23(2).

[9] Kong Q, Zhu J, Ho SCM and Song G. Tapping and listening: a new approach to bolt looseness monitoring. *Smart Mater Struct*. 2018;27(7):07LT02.

[10] Yuan R, Lv Y, Kong Q and Song G. Percussion-based bolt looseness monitoring using intrinsic multiscale entropy analysis and BP neural network. *Smart Mater Struct*. 2019;28(12):125001.

[11] Wang F, Ho SCM and Song G. Modeling and analysis of an impact-acoustic method for bolt looseness identification. *Mech Syst Signal Process*. 2019;133:106249.

[12] Wang T, Tan B, Lu G, Liu B and Yang D. Bolt pretightening force measurement based on strain distribution of bolt head surface. *J Aerosp Eng*. 2020;33:04020034.

[13] Deng S, Wang T, Tan B, Yu W and Lu G. Proof-of-concept study of bolt connection status monitoring using fiber Bragg grating curvature sensor. *Smart Mater Struct*. 2022; DOI:10.1088/1361-665X/ac9566.

[14] Sanvito S, Passoni M, Giusti D, Terenzi M, Prelini C, La Mura M and Savoia AS. PMUT-based system for continuous monitoring of bolted joints preload. *Sensors*. 2024;24:4150.

[15] Wang C, Wang N, Ho SC, Chen X and Song G. Design of a new vision-based method for the bolts looseness detection in flange connections. *IEEE Trans Ind Electron*. 2019;67(2):1366–1375.

[16] Luo J, Li K, Shi B, Chen S, Wu Y and Cheng L. Anti-loosening bolt looseness diagnosis method for flange node based on quick response code. *Sci Rep*. 2025;15:41124.

[17] Kong X, Liu J, Liu Z, He W, Liu G, Li S, Zhao D and Zhang J. Quantitative identification of bolt loosening based

on image feature point matching and deep learning. *Eng Appl Artif Intell*. 2026; (in press).

[18] Jiang J, Ho SCM, Tippitt T, Chen Z and Song G. Feasibility study of a touch-enabled active sensing approach to inspecting subsea bolted connections using piezoceramic transducers. *Smart Mater Struct*. 2020;29(8):085038.

[19] Sanli A, Demirkale B and Kanoun O. Real-time detection of loosening torque in bolted joints using piezoresistive pressure-sensitive layer based on multi-walled carbon nanotubes reinforced epoxy nanocomposites. *Sci Rep*. 2025;15:4830.

[20] Wang F, Chen Z and Song G. Monitoring of multi-bolt connection looseness using entropy-based active sensing and genetic algorithm-based least square support vector machine. *Mech Syst Signal Process*. 2020;136:106507.

[21] Wang T, Zhang S, Yuan R, Tan B and Lu M. Lead Zirconate Titanate-based bolt looseness monitoring using multiscale singular spectrum entropy analysis and genetic algorithm-based support vector machine. *Proc Inst Mech Eng Part C J Mech Eng Sci*. 2024;238(13):6256–6268.

[22] Wang F, Chen Z and Song G. Smart crawfish: a concept of underwater multi-bolt looseness identification using entropy-enhanced active sensing and ensemble learning. *Mech Syst Signal Process*. 2021;149:107186.

[23] He S, Chen J, Chen Z and Song G. An exploratory study of underwater bolted connection looseness detection using percussion and a shallow machine learning algorithm. *Acta Mech Sin*. 2023;39(4):722360.

[24] Chen Y, Zhu L, Gao Z, Li W and Wu J. Multi-bolt looseness positioning using multivariate recurrence analytic active sensing method and MHAMCNN model. *Struct Health Monit*. 2025;24:812–829.

[25] Qin M, Xie Z, Xie J, Yu X, Ma Z and Wang J. Automated structural bolt micro looseness monitoring method using deep learning. *Sensors*. 2024;24(22):7340.

[26] Zhang X, Xia Y and Zhao J. Intelligent identification of bolt looseness with one-dimensional deep convolutional neural networks. *Signal Image Video Process*. 2025;19:158.

[27] Chen J, Chen Z, Zhu W and Song G. Underwater bolted flange looseness detection using percussion-induced sound and Feature-reduced Multi-ROCKET model. *Struct Health Monit*. 2024;23(1):495–511.

[28] Bao Y and Li H. Machine learning paradigm for structural health monitoring. *Struct Health Monit*. 2021;20(4):1353–1372.

[29] Gardner P, Liu X and Worden K. On the application of domain adaptation in structural health monitoring. *Mech Syst Signal Process*. 2020;138:106550.

[30] Gardner P, Bull LA, Gosliga J, Poole J, Dervilis N and Worden K. A population-based SHM methodology for heterogeneous structures: transferring damage localisation knowledge between different aircraft wings. *Mech Syst Signal Process*. 2022;172:108918.

[31] Giglioni V, Poole J, Venanzi I, Ubertini F and Worden K. A domain adaptation approach to damage classification with an application to bridge monitoring. *Mech Syst Signal Process*. 2024;209:111135.

[32] Giglioni V, Poole J, Mills R, Venanzi I, Ubertini F and Worden K. Transfer learning in bridge monitoring: laboratory study on domain adaptation for population-based SHM of multispan continuous girder bridges. *Mech Syst Signal Process*. 2025;224:112151.

[33] Battu RS, Agathos K, Londoño Monsalve JM, Worden K and Papatheou E. Combining transfer learning and numerical modelling to deal with the lack of training data in data-based SHM. *J Sound Vib*. 2025;595:118710.

[34] Chen Y, Wei J, Gao Z, Li W and Wu J. Multibolt looseness monitoring of steel structure based on multitask active sensing method and substructure cross-domain transfer learning. *Struct Health Monit*. 2024;23(6):3486–3504.

[35] Shaw H, Chen J and Song G. Few-shot centroid alignment domain adaptation (CADA) approach to air-to-water transfer learning in smart touch-based bolted flange looseness detection. 2026. Preprint.

[36] Ganin Y, Ustunova E, Ajakan H, Germain P, Larochelle H, Laviolette F, Marchand M and Lempitsky V. Domain-adversarial training of neural networks. *J Mach Learn Res*. 2016;17(1):2096–2030.